

## Research Article

# Research on Multijoint Rock Failure Mechanism Based on Moment Tensor Theory

J. F. Chai <sup>1,2</sup>

<sup>1</sup>Railway Engineering Research Institute, China Academy of Railway Sciences Corporation Limited, Beijing 100081, China

<sup>2</sup>State Key Laboratory for Track Technology of High-Speed Railway, China Academy of Railway Sciences Corporation Limited, Beijing 100081, China

Correspondence should be addressed to J. F. Chai; [chaijinfei@rails.cn](mailto:chaijinfei@rails.cn)

Received 21 April 2020; Accepted 4 May 2020; Published 8 August 2020

Guest Editor: Miaojuan Peng

Copyright © 2020 J. F. Chai. This is an open access article distributed under the Creative Commons Attribution License, which permits unrestricted use, distribution, and reproduction in any medium, provided the original work is properly cited.

To reveal the influence of the number and location of joints on rock failure mechanism, using Particle Flow Code (PFC) to simulate the calculation of a large amount of acoustic emission data generated during breeding, development, and penetration of rock cracks, the fracture parameters such as the spatial location, rupture azimuth, rupture type, stress state, and moment magnitude of acoustic emission events in various fracture stages of multijoint rock were studied based on the moment tensor theory, the P-T diagram method, and the T-k diagram method. It will be of great importance in the geotechnical engineering field.

## 1. Introduction

Acoustic emission (AE), which is a phenomenon of rapid release of strain energy causing the produce of transient elastic waves, is generated spontaneously by plastic deformation and microfailures initiation and growth when a rock is influenced by external force, internal force, or temperature [1]. Through the computation analysis of rupture parameters and rupture types during rock failure, the procedure can reveal the mechanisms of rock failure and judge the evolution law. Therefore, analyzing the mechanisms of rock failure has important theoretical significance and application value.

Kaiser conducted a study of materials acoustic emission characteristics in 1950, which was the origin of modern acoustic emission techniques [2]. Recently, many domestic and international scholars have carried out lots of research studies in rock engineering, mostly concentrating on studying the theory and application of experiments about Kaiser Effect and the law of AEs when a rock is subjected to sufficient load until damage. Liu analytically investigated the friction effect on the buckling behaviors of cellular structures under axial load [3, 4]. Cheng introduced a meshless method based on the nonsingular weight functions for elastoplastic large deformation problems [5, 6]. Ishida researched the acoustic emission monitoring of hydraulic fracturing in laboratory and field [7]. Landis

researched the micro-macro-fracture relationships and acoustic emissions in concrete [8]. Ohtsu researched the crack classification and moment tensor based on acoustic emission [9, 10]. Muralidhara researched the fracture process zone size and true fracture energy of concrete using acoustic emission [11]. On the basis of studying the uniaxial compression test of granite, He et al. analyzed the frequency characteristics of acoustic emission signals during different stages of rock failure process [12]. In the application field, Li utilized Kaiser Effect of rock acoustic emissions to determine the values and directions of the three principal stresses of surrounding rock in deep mining [13]. Gilbert first introduced the concept of moment tensor, which he defined as the first moment of equivalent volume force, to represent a point source [14].

Ji analyzed frequency characteristics of AE at the stage of rock failure by using uniaxial compression tests of granite [15]. Under the utilization of AE system, the regulation and characteristics of AE with stress and time were researched by Zhao [16–18]. The source was represented by the moment tensor. And displacement of far field expressed by moment tensor was linear without the assumption of source mechanism [19]. Initially, moment tensor was applied to rock engineering and rock mechanical test. And types of rock failures were researched using moment tensor in Foreign Countries. At URL, moment tensor was introduced to

analyze the types of fracture at the source by Feignier, to explain the tensile fracture located in the spandrel during the process of drilling with machine. Moment tensor was divided into isotropic part ( $M^{\text{ISO}}$ ) and deviator part ( $M^{\text{dev}}$ ). Types of fracture at the source were quantified by the ratio of isotropic part ( $M^{\text{ISO}}$ ) to the entire moment tensor [20]. Based on the ratio shear component of eigenvalue of moment value to the entire, fracture types of AE were judged, and location of fracture plane of AE was determined. Using PFC and PFC3D, failure of rock was simulated, and moment tensor was calculated by Hazzard [21, 22]. And Hazzard described fracture source mechanism of microseism by using types of fractures introduced by Feignier. Based on the results of moment decomposition method in the same maximum axial direction, Cao explained the application of moment tensor in the judgment of types of rock failure and simulated reliability and applicability of moment tensor in the analysis of types of mining induced rock and coal fracture by using theory method [23]. Chai judged the types of fracture in the mining microseism by moment tensor, analyzed the applicability of moment tensor in engineering [24], and studied the internal fracture mechanism of simulated rock acoustic emission events using T-k diagram method and P-T graph method [25–27]. Cheng researched the element-free Galerkin method based on the nonsingular weight functions [28–31].

Moment tensor has been applied in geotechnical engineering for 20 years; however, the number of researches using moment tensor in analysis of rock failure types is still very small, especially in the field of rock fracture mechanism and evolution rule; there is scarcely any related research work. Therefore, this paper utilizes Particle Flow Code (PFC) and moment tensor inversion method to obtain some parameters of rock failure events, such as spatial position, moment magnitude, moment tensor, T-k value, and rupture orientations, and conducts a quantitative research on the rock fracture mechanism and evolution rule. It will be of great importance in geotechnical engineering field.

## 2. Simulation Method

**2.1. PFC Simulative Approach.** In PFC simulative approach, the displacement triggered by the total contact forces, which act on the surfaces of particles, can be equivalent to the same effect, namely, the moment tensor, triggered by volumetric forces.

The two particles on either side of the failure can be defined as source particles. After the bond between them breaks, the source particles will move, and contacts surrounding the source particles will suffer some deformation. The contact force will, therefore, change due to the formation of the failure. The action zone of the microfailure is a circle with the centre of the circle being the microfailure centroid, and the radius is the maximum particle diameter. Then an summation operation around the contacts surrounding the failure can be performed to calculate components of the moment tensor as

$$M_{ij} = \sum \Delta F_i R_j, \quad (1)$$

where  $\Delta F_i$  is the  $i$  th component change in contact force, and  $R_j$  is  $j$  th component of the distance between the contact point and the event centroid.

Combined with equation (2), the moment magnitude  $M_w$  can be calculated from the peak scalar moment by

$$M_0 = \left( \sum_{j=1}^3 \left( \frac{m_j^2}{2} \right) \right)^{1/2}. \quad (2)$$

Combined with equation (2), the moment magnitude  $M_w$  can be calculated from the peak scalar moment by

$$M_w = \frac{2}{3} \log M_0 - 6. \quad (3)$$

**2.2. Moment Tensor Decomposition.** Moment tensor of rock rupture is a second-order symmetric tensor, and all of its three principal eigenvalues are real, and there exist three orthogonal principal axes, namely, three eigenvectors. Assume that the three principal eigenvalues of moment tensor are  $M_x \geq M_z \geq M_y$ , and the corresponding three eigenvectors are  $t, b, p$ . In principal axial system, moment tensor can be diagonalized and decomposed as [14]

$$\begin{aligned} M &= \begin{bmatrix} M_{xx} & M_{xz} & M_{xy} \\ M_{zx} & M_{zz} & M_{zy} \\ M_{yx} & M_{zy} & M_{yy} \end{bmatrix} = \begin{bmatrix} M_x & 0 & 0 \\ 0 & M_z & 0 \\ 0 & 0 & M_y \end{bmatrix} \\ &= \frac{1}{3} M_x + M_z + M_y \begin{bmatrix} 1 & 0 & 0 \\ 0 & 1 & 0 \\ 0 & 0 & 1 \end{bmatrix} + \begin{bmatrix} M'_x & 0 & 0 \\ 0 & M'_z & 0 \\ 0 & 0 & M'_y \end{bmatrix} \quad (4) \\ &= M^{\text{ISO}} + M', \end{aligned}$$

$$M'_i = M_i - M^{\text{ISO}} = M_i - \frac{1}{3} (M_x + M_z + M_y), \quad (5)$$

where  $M'_i$  are deviatoric moments,  $i = x, y, z$ .

One of the simplest decomposition methods is to determine the isotropic part and deviatoric part of moment tensor. If the isotropic part is positive, the rupture type is tension failure (uniform explosion), while if it is negative, the rupture type will be pressure failure (uniform implosion). And the proportions of two parts, respectively, take the form as [32]

$$\% \text{DEV} = 100 - \% \text{ISO}, \quad (6)$$

$$\% \text{ISO} = \frac{M_{\text{ISO}}}{|M_{\text{ISO}}| + \sum |M'_i|} \times 100. \quad (7)$$

If the proportion of isotropic part is greater than 30%, it can be considered that the event has obvious isotropic part. But one thing that should be noted in the two-dimensional coordinate department is that the maximum value of

isotropic part is 66% because one of the eigenvalues is equal to zero.

**2.3. T-k Plot Method.** Hudson (1989) has come up with two parameters T and k of moment tensor to analyze the source rupture type. The parameter T is used to measure deviatoric part of source with its range from pure positive CLVD, which is located at -1, to pure negative CLVD, located at +1, crossing the pure DC located at original point. The parameter k is used to measure isotropic part with its range from uniform explosive type located at +1 to uniform implosive type located at -1.

As shown in Figure 1, these two parameters can be drawn into an equal area source type plot. Assuming  $M_x \geq M_z \geq M_y$  are the three eigenvalues of moment tensor, then T and k can be presented as

$$k = \frac{M_{\text{ISO}}}{|M_{\text{ISO}}| + \max(|M'_x|, |M'_y|)}, \quad (8)$$

$$T = \frac{2M'_z}{\max(|M'_x|, |M'_y|)}. \quad (9)$$

**2.4. P-T Plot Method.** Through calculating the moment tensor of acoustic emission and using the equation (10), we can get the fracture azimuth information, which contains the pure Double Couple component of moment tensor:

$$\begin{cases} M_{11}^{\text{DC}} = -M_0 (\sin \delta \cos \lambda \sin \varphi_s + \sin 2\delta \sin \lambda \sin^2 \varphi_s), \\ M_{12}^{\text{DC}} = M_{21}^{\text{DC}} = M_0 \left( \sin \delta \cos \lambda \sin \varphi_s + \frac{1}{2} \sin 2\delta \sin \lambda \sin 2\varphi_s \right), \\ M_{13}^{\text{DC}} = M_{31}^{\text{DC}} = -M_0 (\cos \delta \cos \lambda \cos \varphi_s + \cos 2\delta \sin \lambda \sin \varphi_s), \\ M_{22}^{\text{DC}} = M_0 (\sin \delta \cos \lambda \sin 2\varphi_s - \sin 2\delta \sin \lambda \cos^2 \varphi_s), \\ M_{23}^{\text{DC}} = M_{32}^{\text{DC}} = -M_0 (\cos \delta \cos \lambda \sin \varphi_s - \cos 2\delta \sin \lambda \cos \varphi_s), \\ M_{33}^{\text{DC}} = M_0 \sin 2\delta \sin \lambda. \end{cases} \quad (10)$$

A single source fracture azimuth can be expressed as the beach ball generally, as shown in Figure 2. Figure 2(a) visually shows the rock fracture azimuth information in the 3D coordinate system (Strike  $\varphi_s$ , Dip  $\delta$ , Slide  $\lambda$ ). Figure 2(b) is the stereographic projection shadow from the lower hemisphere to the equatorial plane of 3D beach ball. In Figure 3, P-axis and T-axis, respectively, represent compressive stress axis and tensile stress axis. A1 is shear fracture surface, and A2 is its orthogonal auxiliary plane. Their intersecting line is zero-axis (B axis). Figure 4 is the two-dimensional beach ball of shear fracture type, tensile rupture type, mixed type, and its stress field distribution.

In order to research the change law of fracture azimuth of a large number of acoustic emission events during rock triaxial compression, the P-axis and T-axis of fracture surface are projected to the equatorial plane (W-N-E-S plane) in this paper. Then, the stereographic projection of P-axis (shown as +) and T-axis (shown as •) is obtained, which is called P-T distribution diagram for short [33].

**2.5. Uniaxial Compression Test of Multijoint Rock.** To reveal the effect of joint number and position to the mechanism of rock fracture, this paper simulated and computed a large amount of acoustic emission data of the process of the generation, growth, and coalescence of rock cracks using PFC (Particle Flow Code) software and then researched the failure parameters of acoustic emission incidents and the their evolution law such as spatial position, failure orientation, failure mode, stress state, and moment magnitude in each stage of multijoint rock failure based on moment tensor theory, the methods of P-T diagram and T-k diagram.

### 3. Calculation Model

This paper uses moment tensor inversion theory to calculate the failure process of the sample simulated on the condition of different joint numbers and positions. In order to research the failure mechanism of rock under uniaxial compression under the condition of different joint numbers and positions, we assume that the medium parameters of imitation specimen are isotropic.

The dimension and loading direction of imitation specimen in this paper are the same as the actual rock samples ( $R$  (X-Y plane) = 50 mm,  $H$  (Z-axis) = 100 mm, the vertical of Z-axis is the loading direction), and the bonding mode between particles is the parallel bond model.

The microparameters (see Table 1) basically agree with the mechanical parameters (see Table 2) of Lac du Bonnet granite sample.

To quantitatively describe the location, orientation, and location of each joint of each rock sample, making the following definition for now (as shown in Figure 5), joint orientation angle for the angle of joint orientation and Z-axis (the direction of compression), joint length  $b = 20$  mm, joint spacing can be expressed as symbol  $c$ .

More than 10 groups of rock failure tests with different multijoints are simulated by PFC in this paper. The joint parameters of rock specimens are shown in Table 3 and Figure 6. The results are shown in Figure 7.

The whole simulated stress-strain curve results in the condition of different numbers and positions of joints are shown in Figure 8. The characteristics of every stage of the curve for the rock sample failure are crack closure stage (O-A), linear elastic stage (A-B), crack initiation stage (B-C), crack increase stage (C-D), large deformation and cumulative damage stage (D-E), peak stress (point D), and residual stress (point E), respectively. According to the results of the acoustic emission simulation and stress-strain curve of rock failure, the initial cracks of every sample are generated at point B, the initial failure stresses are 89.94 Mpa, 85.28 Mpa,

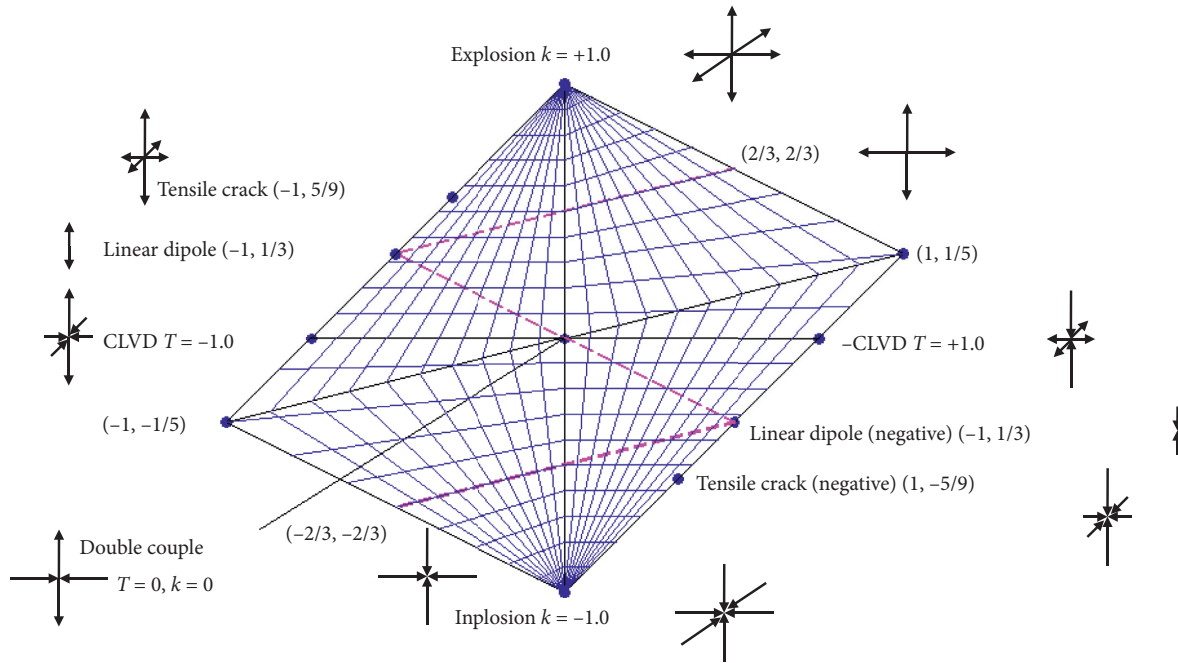


FIGURE 1: The T-k distribution diagram.

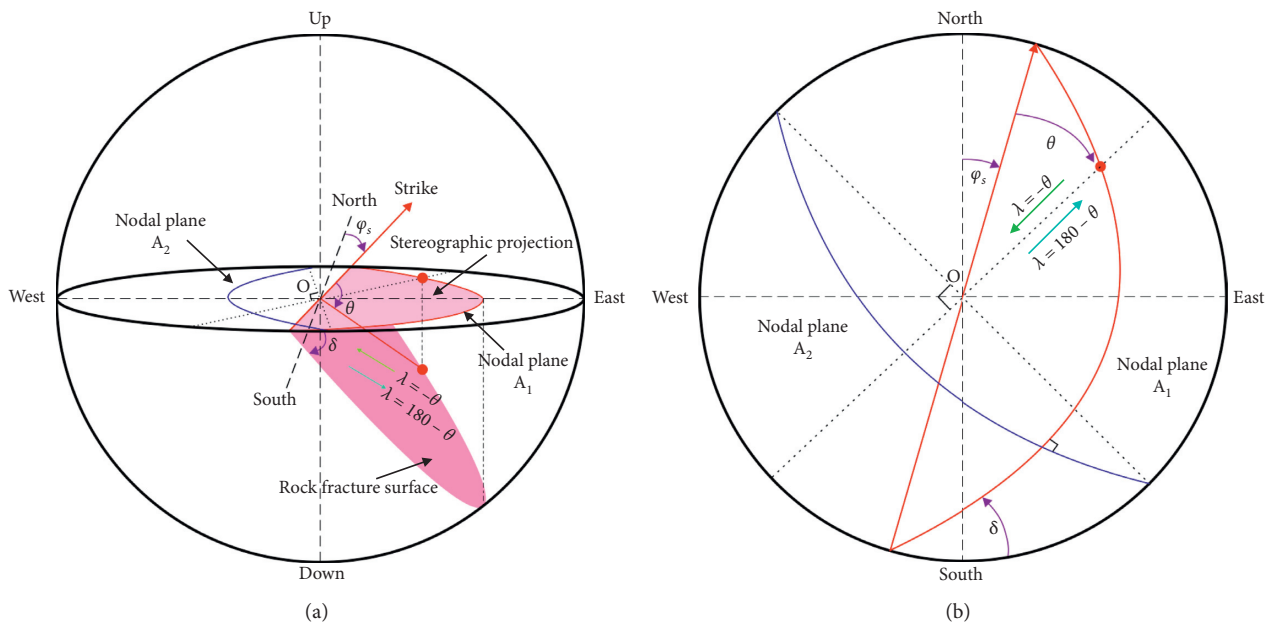


FIGURE 2: The interpret Figures of beach ball. (a) Three-dimensional beach ball. (b) Two-dimensional beach ball.

81.26 Mpa, 79.9 Mpa, 72.15 Mpa, 74.16 Mpa, 75.08 Mpa, 78.89 Mpa, 79.36 Mpa, and 82.12 Mpa, the peak stresses are 181.90 Mpa, 173.10 Mpa, 170.70 Mpa, 162.50 Mpa, 164.20 Mpa, 168.20 Mpa, 159.50 Mpa, 163.60 Mpa, 156.40 Mpa, and 165.50, and the strains in peak stress are  $3.124 \times 10^{-3}$ ,  $2.916 \times 10^{-3}$ ,  $2.925 \times 10^{-3}$ ,  $2.703 \times 10^{-3}$ ,  $2.806 \times 10^{-3}$ ,  $2.902 \times 10^{-3}$ ,  $2.774 \times 10^{-3}$ ,  $2.945 \times 10^{-3}$ ,  $2.723 \times 10^{-3}$ , and  $2.980 \times 10^{-3}$ , respectively.

By analyzing the axial stress and strain difference values of the rock specimens at peak stress, some rules can be summarized as follows:

- (1) As the green arrows shown in Figures 9 and 10, the axial stress difference values and the axial strain difference values of rock specimens decrease with the increase of the joint orientation angle ( $\alpha$ ) comparing Sample 30-2, Sample 45-2-1, Sample 45-2-2, and Sample 60-2.
- (2) As the blue arrows shown in Figure 9 and the orange arrows shown in Figure 10, the axial stress difference values and the axial strain difference values of multijoints rocks (Sample 45-3-1, Sample 45-4-1, and Sample 45-5-1) with Joint Type 2 are less than

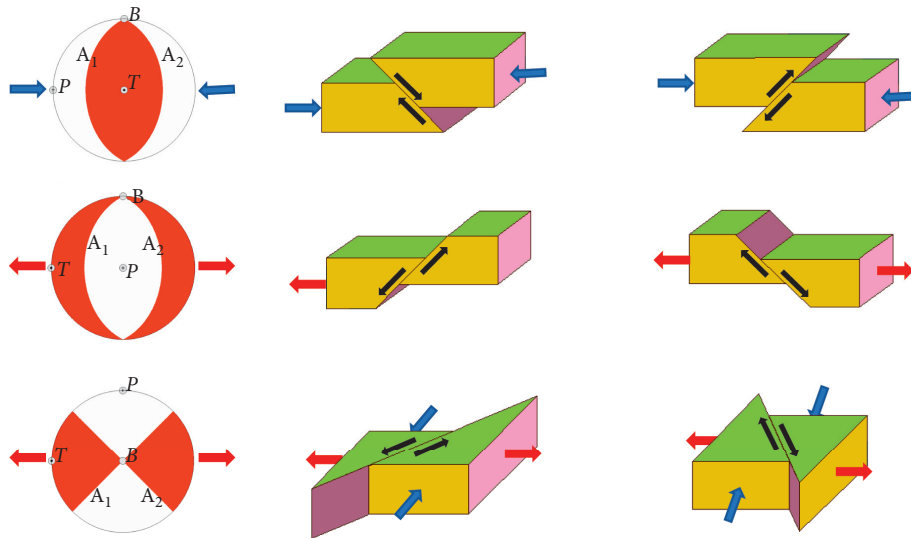


FIGURE 3: The stress field distribution of beach ball.

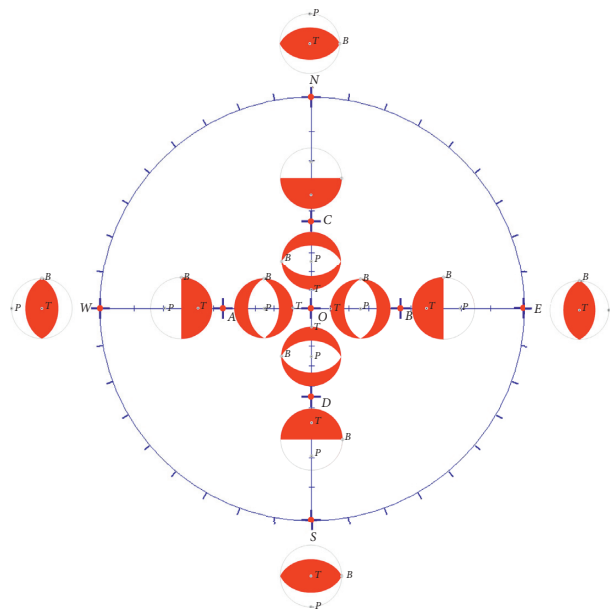


FIGURE 4: The P-T distribution diagram.

TABLE 1: Mechanical parameters of parallel bond model.

Radius of minimum particle $R_{min}$ (mm)	Radius ratio of max-min particle	Density $\rho$ ( $\text{kg}\cdot\text{m}^{-3}$ )	Interparticle friction coefficient $\mu$	Elastic modulus $E_c$ (MPa)	Normal-tangential stiffness ratio $(k_n/k_s)$	
0.50	1.66	2630	0.50	67000	2.5	
Radius coefficient $\lambda$	Elasticity modulus $\bar{E}_c$ (MPa)	Normal-tangential stiffness ratio $(\bar{k}_n/\bar{k}_s)$	Average value $\sigma_{n\text{-mean}}$ (MPa)	Standard deviation $\sigma_{n\text{-dev}}$ (MPa)	Average value $\tau_{s\text{-mean}}$ (MPa)	Standard deviation $\tau_{s\text{-dev}}$ (MPa)
1.0	67000	2.5	166	$\pm 38$	166	$\pm 38$

TABLE 2: Mechanical parameters of Lac du Bonnet granite.

Elastic modulus $E_c$ (MPa)	Uniaxial compressive strength (MPa)	Poisson's ratio	P-wave velocity ( $\text{m}\cdot\text{s}^{-1}$ )	S-wave velocity ( $\text{m}\cdot\text{s}^{-1}$ )
67031	48 ~ 210	0.25	5820	3360

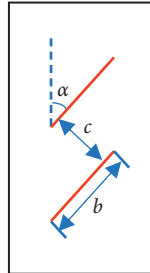


FIGURE 5: Interpretation diagram of joint orientation.

TABLE 3: Joint parameters of rock specimens.

Sample number					
Joint parameters	30-2	45-2-1	45-2-2	60-2	45-3-1
Number of joints (number)	2	2	2	2	3
Joint orientation $\alpha$ ( $^\circ$ )	30	45	45	60	45
Joint spacing $c$ (mm)	10	10	30	10	20
Joint mode	Mode 1	Mode 1	Mode 3	Mode 1	Mode 2
Sample number					
Joint parameters	45-3-2	45-4-1	45-4-2	45-5-1	45-5-2
Number of joints (number)	3	4	4	5	5
Joint orientation $\alpha$ ( $^\circ$ )	45	45	45	45	45
Joint spacing $c$ (mm)	15	13.3	10	10	7.5
Joint spacing	Mode 3	Mode 2	Mode 3	Mode 2	Mode 3

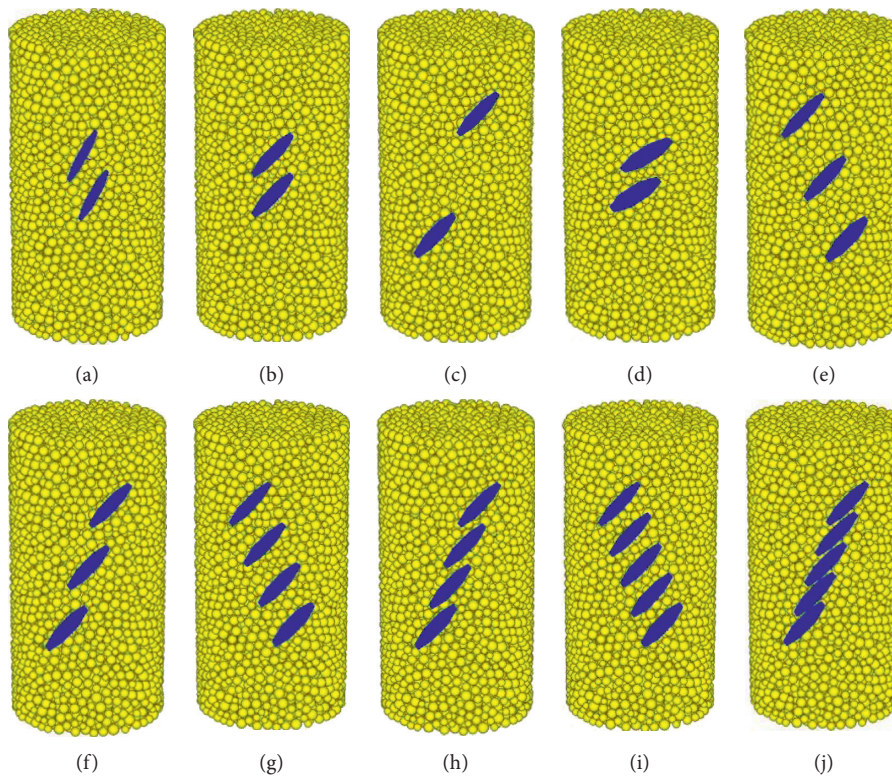


FIGURE 6: Joint orientation of rock specimens: (a) 30-2, (b) 45-2-1, (c) 45-2-2, (d) 60-2, (e) 45-3-1, (f) 45-3-2, (g) 45-4-1, (h) 45-4-2, (i) 45-5-1, and (j) 45-5-2.

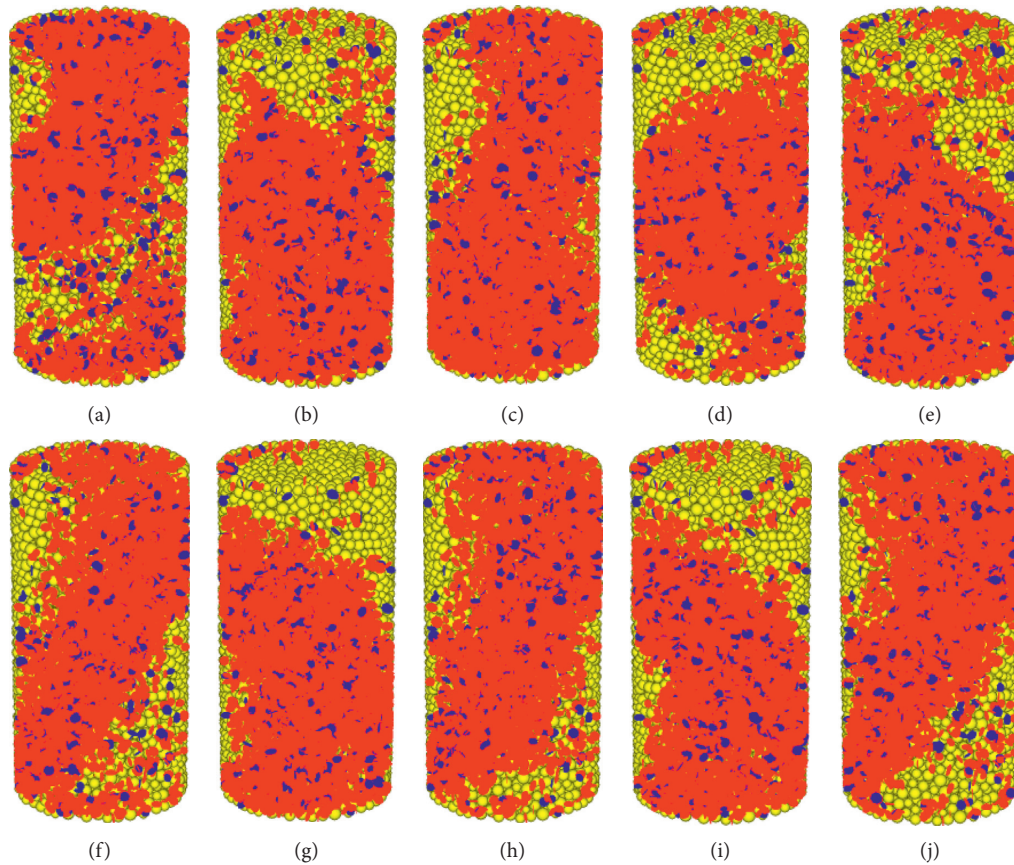


FIGURE 7: Simulated result by PFC software: (a) 30-2, (b) 45-2-1, (c) 45-2-2, (d) 60-2, (e) 45-3-1, (f) 45-3-2, (g) 45-4-1, (h) 45-4-2, (i) 45-5-1, and (j) 45-5-2.

those of the rock specimen (Sample 45-3-2, Sample 45-4-2, and Sample 45-5-2) with Joint Type 3 when the number of joints is the same.

- (3) As the yellow arrows shown in Figures 9 and 10, the axial stress and strain difference values decrease with the increase in the number of joints when the joints of rock specimens are Joint Type 2 (Sample 45-3-1, Sample 45-4-1, and Sample 45-5-1).
- (4) As the purple arrows shown in Figure 10, the axial stress difference values first decrease and then slightly increase with the increase in the number of joints when the joints of rock specimens are Joint Type 3 (Sample 45-3-2, Sample 45-4-2, and Sample 45-5-2). This phenomenon is related to stress fluctuation caused by the large-scale failure at the peak stress.
- (5) As the cyan arrows shown in Figure 9, the axial strain difference values decrease with the increase in the number of joints when the joints of rock specimens are Joint Type 3 (Sample 45-3-2, Sample 45-4-2, and Sample 45-5-2).
- (6) Before the peak stress, the variation rate of elastic modulus is very small; the curve shows obvious fluctuation at the peak stress and a sharp decline after the peak stress; it means that the rock specimens have strong brittle features.

In the process of rock failure, the simulated results of parameters such as spatial position, failure magnitude, and fracture type of acoustic emission are shown in Figure 11. The shape of acoustic emission events represents its fracture type (the circulars represent the linear tension fracture; the rhombuses represent the linear shear fracture; the squares represent the double couple shear fracture, the hexagons represent the middle mixed fracture with large principal stress). The space size of acoustic emission events represents the scale of moment magnitude.

By analyzing the parameters such as spatial location, moment magnitude, and fracture type of acoustic emission events in the process of rock failure, some rules can be obtained as follows:

- (1) Crack closure stage (O-A) and linear elastic stage (A-B): acoustic emission events have not yet begun to generate
- (2) Crack generation stage (B-C): acoustic emission events begin to appear in the area near the surface of joints and axial load; every fracture types have appeared; these moment magnitudes are very small
- (3) Crack increase stage (C-D): acoustic emission events gradually appear in all over the rock specimen and begin to concentrate in the area near the joints and two axial loading surfaces; these moment magnitudes are still very small; but linear tensile fracture events increase obviously

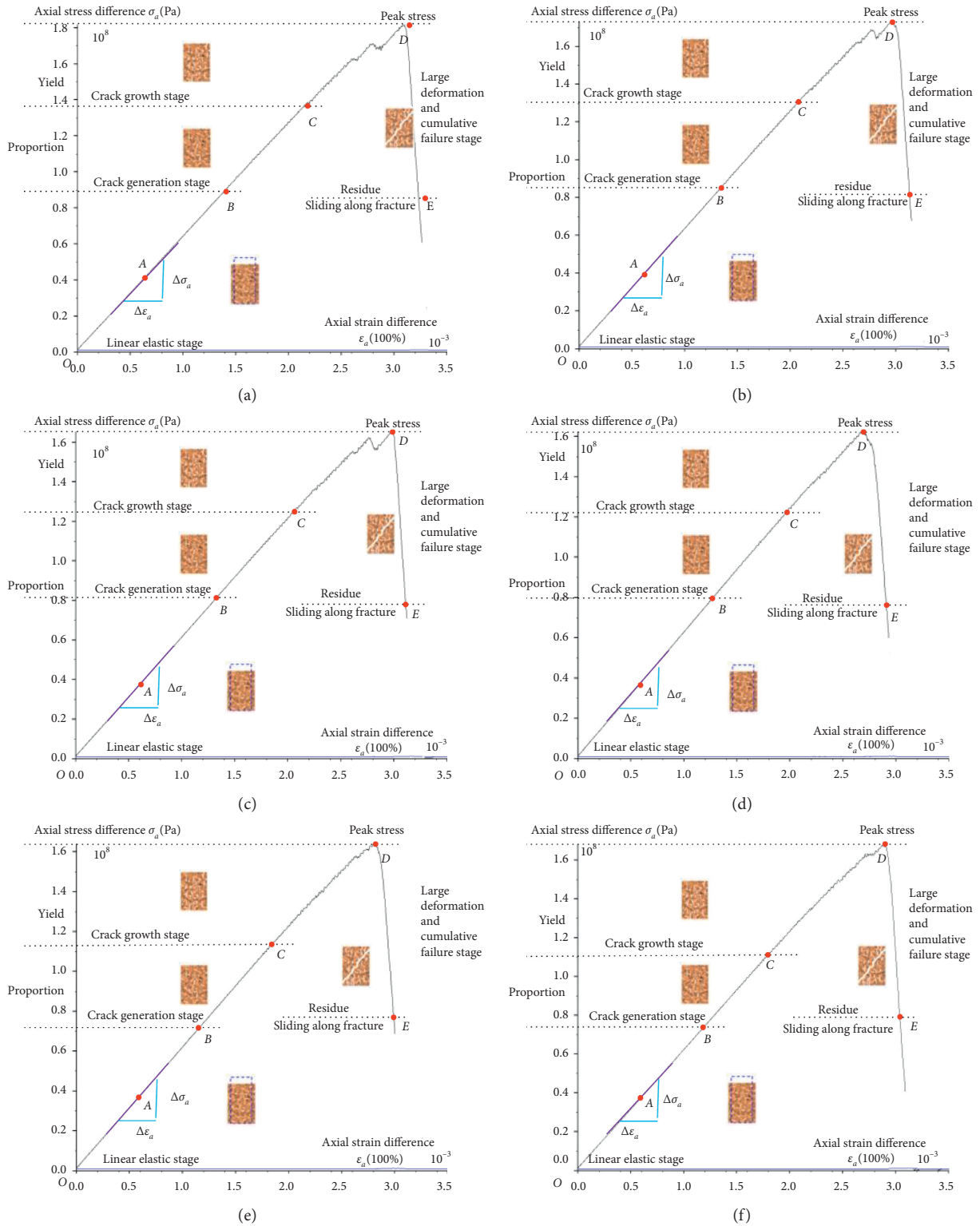


FIGURE 8: Continued.

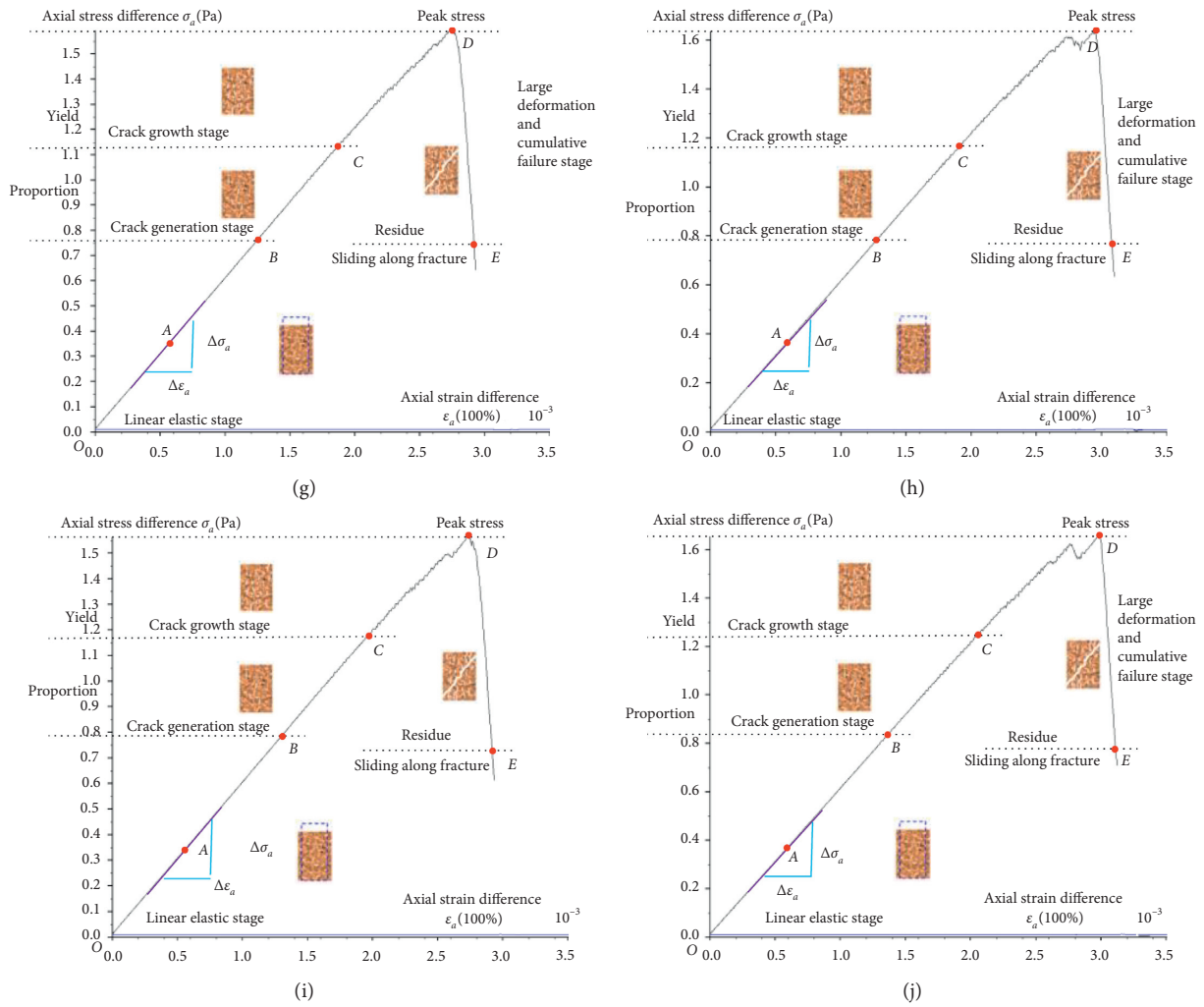


FIGURE 8: Whole stress-strain curve of rock failure process: (a) 30-2, (b) 45-2-1, (c) 45-2-2, (d) 60-2, (e) 45-3-1, (f) 45-3-2, (g) 45-4-1, (h) 45-4-2, (i) 45-5-1, and (j) 45-5-2.

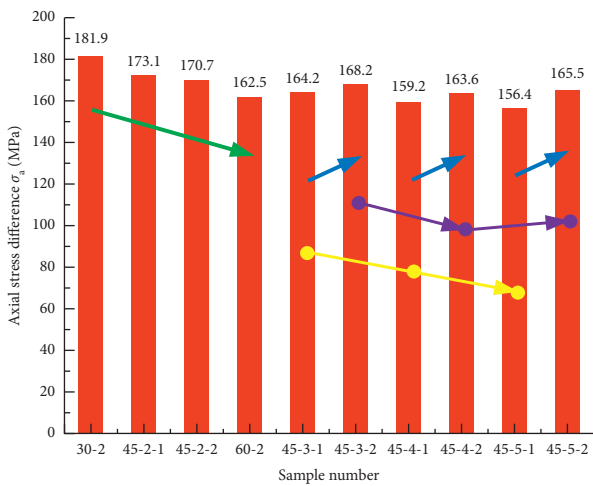


FIGURE 9: Axial stress difference values.

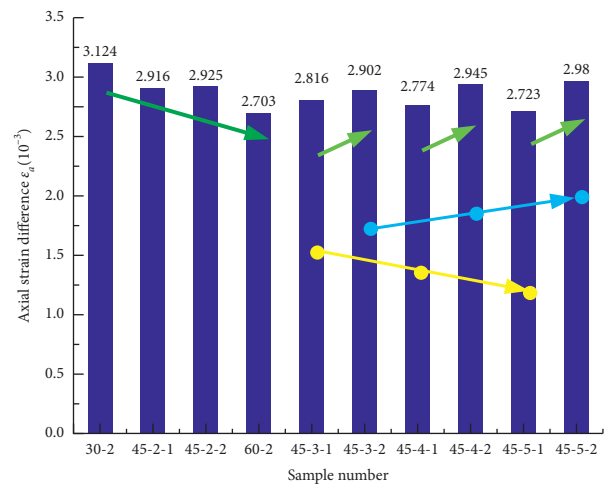


FIGURE 10: Axial strain difference values.

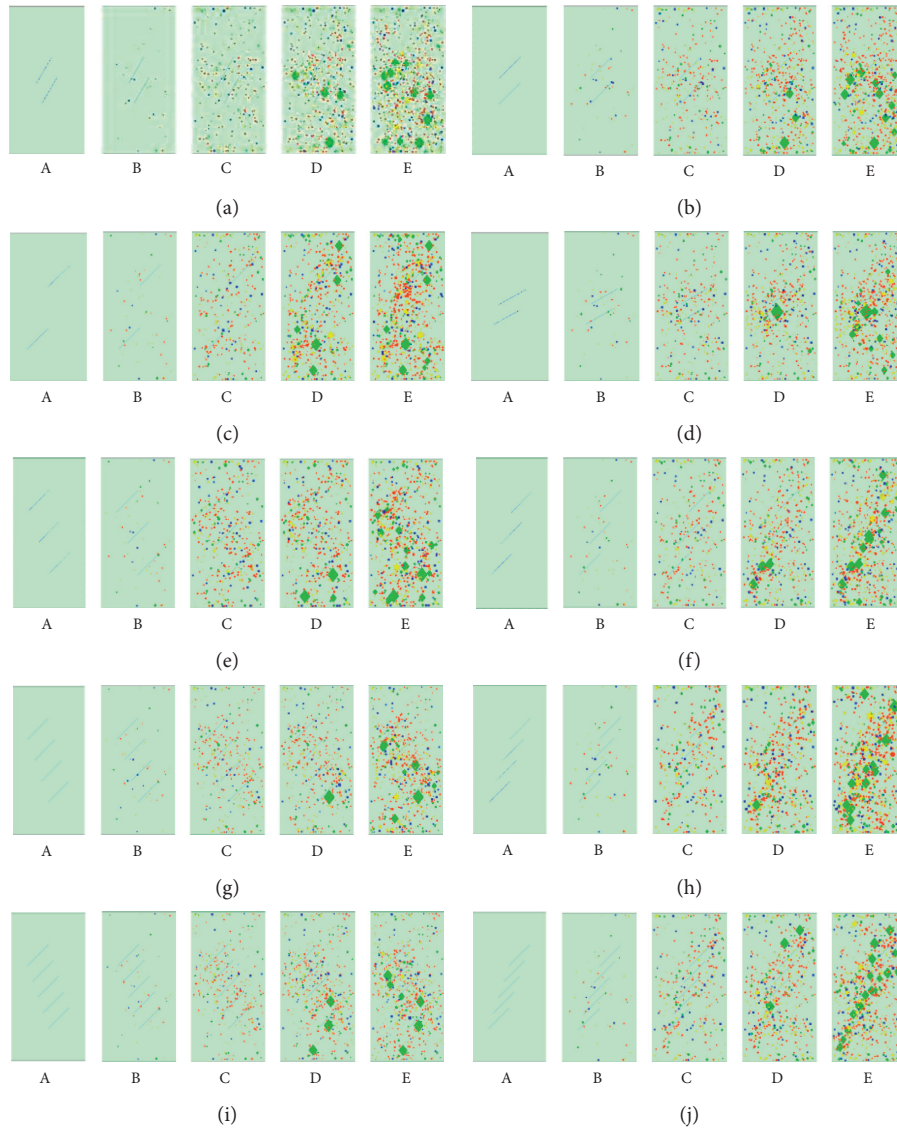


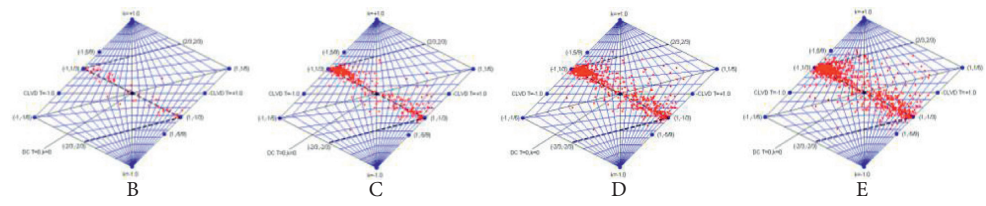
FIGURE 11: Spatial positions of acoustic emission events and calculated results of fracture parameters: (a) 30-2, (b) 45-2-1, (c) 45-2-2, (d) 60-2, (e) 45-3-1, (f) 45-3-2, (g) 45-4-1, (h) 45-4-2, (i) 45-5-1, and (j) 45-5-2.

- (4) Peak stress (point D): acoustic emission events continuously increase, and linear shear fracture events and mixed fracture events with larger moment magnitude begin to appear at the end of each joint and the area between joints and extension direction of joints
- (5) Large deformation and cumulative damage stage (D-E): linear shear failure events and fixed failure events with larger moment magnitude mainly distribute at the end of each joint, along the direction of joints and along the direction of joint sets; when the rock specimens contain two joints, linear shear failure events and fixed failure events mainly distribute the area near joints and along the direction of joints; when the rock specimens contain more joints, if the rock specimens contain Joint Type 2, linear shear failure events and fixed failure events mainly

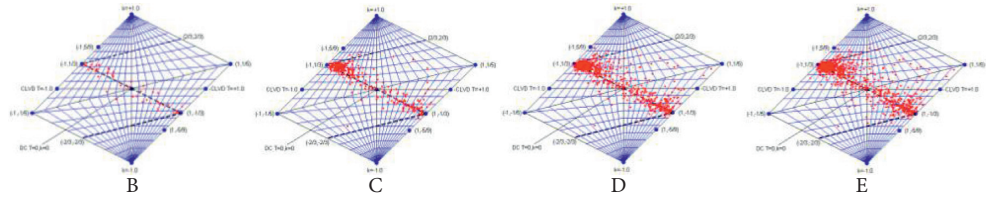
distribute along the direction of two joints, which are located near two axial loading surfaces and the direction of joint sets; if the rock specimen contains Joint Type 3, linear shear failure events and fixed failure events mainly distribute along the direction of joint sets; when the number of joints is the same, linear shear failure events in the rock specimens containing Joint Type 3 are more than those in the rock specimens containing Joint Type 2

**3.1.  $T$ - $k$  Distribution of Moment Tensor.** In the simulation results of rock stress-strain curve as shown in Figure 12, the rock failure mechanism and evolution law in each stage can be analyzed by the distribution of  $T$ - $k$  parameters.

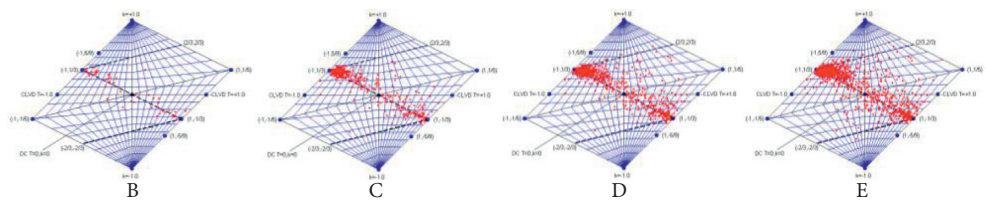
As shown in Figure 12, the distributions and evolution laws of  $T$ - $k$  value points in each rock specimens are very similar:



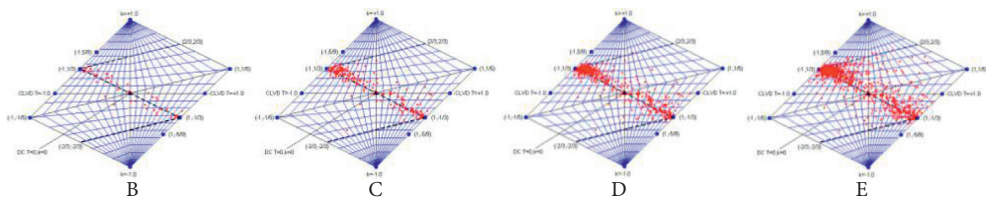
(a)



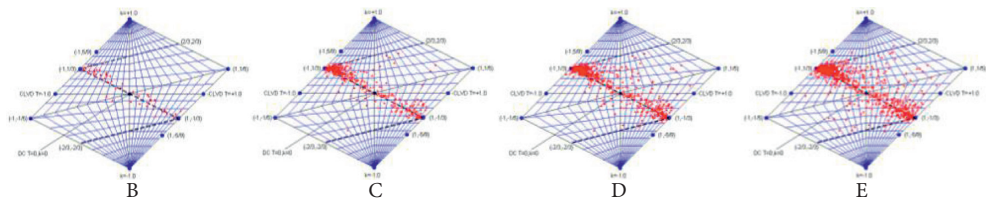
(b)



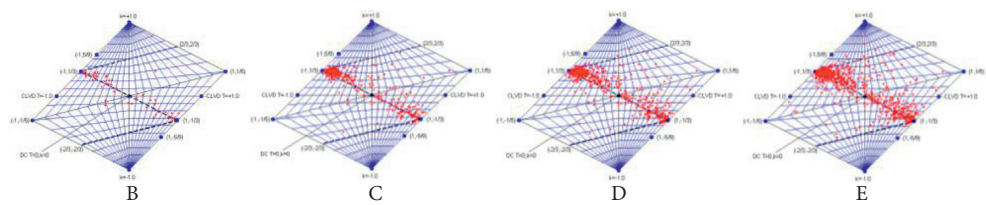
(c)



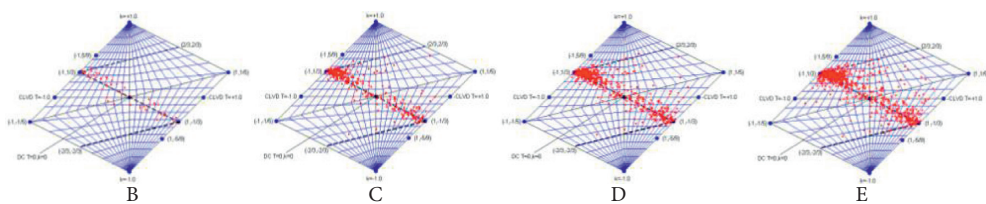
(d)



(e)



(f)



(g)

FIGURE 12: Continued.

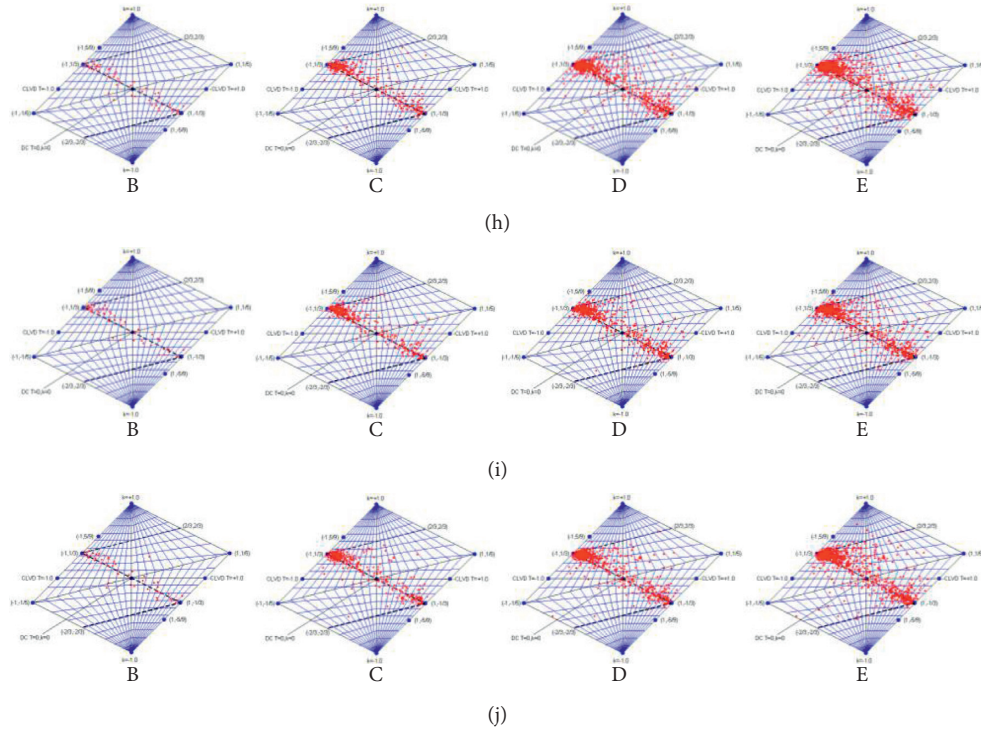


FIGURE 12: T- $k$  distribution diagram of moment tensor: (a) 30-2, (b) 45-2-1, (c) 45-2-2, (d) 60-2, (e) 45-3-1, (f) 45-3-2, (g) 45-4-1, (h) 45-4-2, (i) 45-5-1, and (j) 45-5-2.

- (1) Crack closure stage (O-A) and linear elastic stage (A-B): T- $k$  value points are not yet appearing.
- (2) Crack generation stage (B-C): T- $k$  value points begin to appear in the area near the line:  $y = -1/2x$ .
- (3) Crack increase stage (C-D): T- $k$  value points continue to increase in the area near the line  $y = 1/2x$  and begin to aggregate on the area near the linear vector dipole  $(-1, 1/3)$ , which means that linear tension failure events increase gradually.
- (4) Peak stress (point D): T- $k$  value points continue to aggregate on the area near the linear vector dipole  $(-1, 1/3)$ ; the points located in the area away from the line  $y = 1/2x$  and the point located in the area near by the negative linear vector dipole  $(1, -1/3)$  increase gradually, which means that linear shear failure events and fixed failure events increase gradually.
- (5) Large deformation and cumulative damage stage (D-E): T- $k$  value points mainly concentrate on the area near the linear vector dipole  $(-1, 1/3)$ ; the points gradually increase in the area near the negative linear vector dipole  $(1, -1/3)$  but are always very dispersed; the number of points located in the area away from the line  $y = -x/2$  gradually increases, but the proportion is still small. The above results mean that the main failure type of acoustic emission events is linear tension failure; analyzing Figure 8, linear shear failure events and fixed failure events gradually increase, but the number is fewer and the energy is large; double couple shear failure events are very few;

explosion failure events and implosion failure events have not occurred.

**3.2. P-T Distribution of Moment Tensor.** In the simulation results of rock stress-strain curve, the rock failure mechanism and evolution law in each stage can be analyzed by the locations and moment magnitudes of acoustic emission as shown in Figure 10 and the distribution of T- $k$  parameters as shown in Figure 13.

As shown in Figure 13, P-T value points of moment tensor and the evolution law of stress field of each joint sample are similar:

- (1) Linear elastic stage (O-A), P-T value points are not yet appearing.
- (2) Crack generation stage (B-C), the principle compression stress component (P-axis) has appeared near the A-axis (Point W or Point E), and the poles in point E are arranged regularly pointing upper left  $45^\circ$ , as Box 1 shown in Figure 13; it shows that when acoustic emission events happen, compression stress components are mainly distributed near the direction of axial stress and a part of them gradually points to 45 degrees by the direction of axial stress; the principle tension stress components (T axis) start to appear near the direction of plane X-Y (near line N-S).
- (3) Crack growth stage (C-D), the principle compression stress components (P-axis) gather gradually near Z-

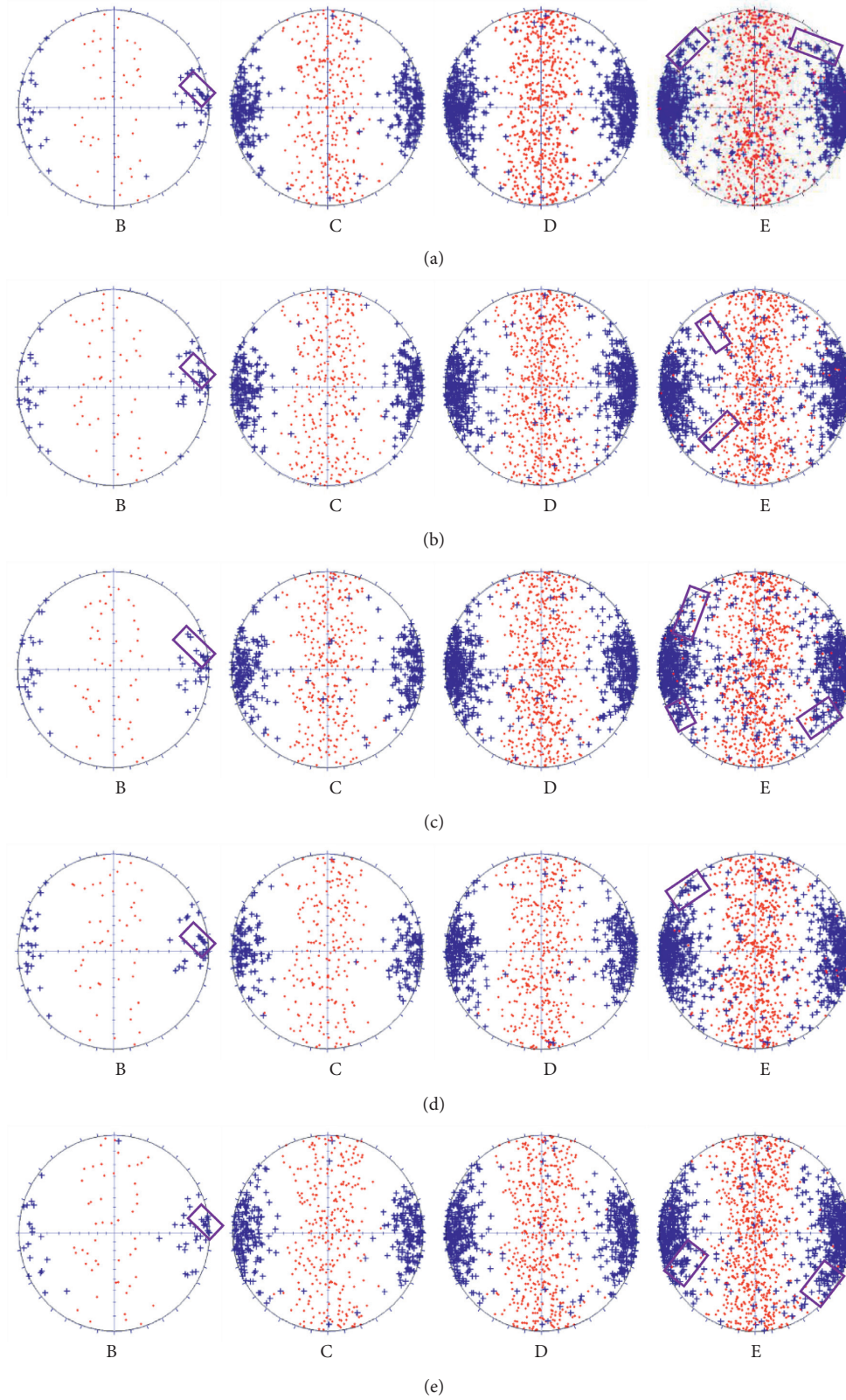


FIGURE 13: Continued.

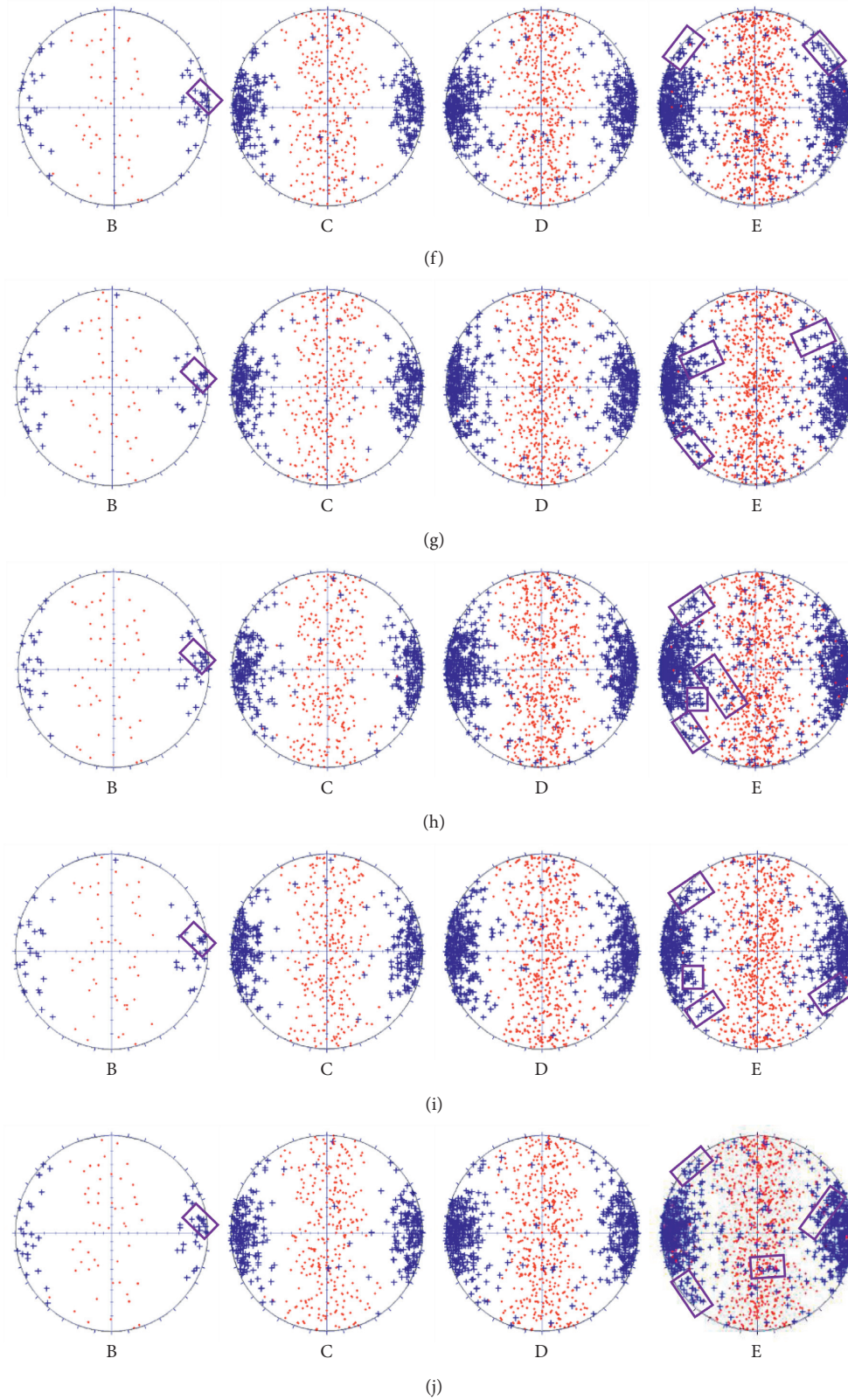


FIGURE 13: P-T distribution diagram of moment tensor: (a) 30-2, (b) 45-2-1, (c) 45-2-2, (d) 60-2, (e) 45-3-1, (f) 45-3-2, (g) 45-4-1, (h) 45-4-2, (i) 45-5-1, and (j) 45-5-2.

axis (point W or point E) and begin to extend to plus or minus 30 degrees by the direction of Z-axis; the principle stress components have increased near the direction of plane X-Y (line N-S) and expand outside gradually.

- (4) Peak stress (point D), the principle compression stress components (P-axis) gather near the area of plus or minus 30 degrees by the direction of Z-axis further and expand outside gradually with regular arrangement in local region; the principle stress components (T-axis) increase further near the direction of plane X-Y and expand outside gradually.
- (5) Large deformation and cumulative damage stage (D-E), the principle compression stress components (P axis) expand from the area of plus or minus 30 degrees by the direction of Z-axis (point W or point E) to the direction of plane X-Y further and finally form an obvious phenomenon of regular arrangement in some local area, and inside each multijoint sample, there are obvious crescent regular arrangements near 30 to 60 degrees by the direction of Z-axis (point W or point E), which illustrates that the multijoint structure can affect the fracture orientation of acoustic emission events to a certain extent; the principle stress components (T-axis) expand from the direction of plane X-Y (line N-S) to Z-axis (point W or point E).

#### 4. Conclusions

By analyzing the complete stress-strain curve, acoustic emission location, failure orientation, failure type, and moment magnitude of multijoint rock compress test in the condition of different numbers and orientation of joints, the following rules are obtained in this paper:

- (1) The axial stress and strain difference values of each multijoint sample decrease with the increase of the angle of the joint and Z-axis.
- (2) When the number of joints is the same, the axial stress and strain difference values of the sample containing type 2 joints are less than those of the rock specimen containing type 3 joints.
- (3) When the joints of rock specimens are of type 2, the axial stress and strain difference values decrease with the increase of the number of joints.
- (4) When the mode of rock specimens joints is of type 3, the axial stress difference values first decrease and then slightly increase with the increase of number of joints, which illustrates that stress fluctuation caused by the large-scale failure before and after peak stress has effect on the difference value, and the axial strain difference values decrease with the increase of number of joints.
- (5) Before the sample reaches the peak stress, the variation rate of the elastic modulus is small; the curve shows obvious fluctuation before the peak stress and a sharp decline after the peak stress,

which shows that the rock specimens have strong brittle features.

- (6) Acoustic emission events first appear near the area containing joints and axial load plane, and all types of failures have appeared, but tension failure is more, and all the moment magnitudes of acoustic emission events are small.
- (7) In peak stress and large deformation stage, the linear shear failure events and fixed failure events with larger moment magnitude are mainly distributed in the end of each joint, along the direction of joints or the joint sets.
- (8) When the sample contains two pieces of joint, the linear shear failure events and fixed failure events are mainly distributed near the joints or in the direction of joint orientation.
- (9) When the rock specimens contain more joints, if the samples contain type two joints, the linear shear failure events and fixed failure events are mainly distributed in the direction of two joints close to the axial loading plane; if the samples contain type three joints, the linear shear failure events and fixed failure events are mainly distributed on the orientation of joint sets.
- (10) When the number of joints is the same, the failures in rock specimen containing type three joints are more than those in the samples containing type two joints.
- (11) First, the points of T-k values first appear and continue to increase near the line  $y = 1/2x$ ; next, the points start to aggregate near the linear vector pair pole  $(-1, 1/3)$ ; the points near the negative linear vector pair pole  $(1, -1/3)$  also increase but are always dispersive; the points away from the line  $y = -1/2x$  increase gradually but are still few. The above shows that the main type of failure is linear tension failure; linear shear failure events and fixed failure events have increased gradually with large energy, but their number is small; double couple shear failure events are few, and homogenic expansion events and homogenic compression failure events have not appeared.
- (12) The principal compressive stress component (P-axis) is first distributed near the direction of the axial stress, and part of the compressive stress components (P-axis) is deflected gradually to 45 degrees by the direction of axial stress; the principal tensile stress components (T-axis) start to appear in the area near the direction of plane X-Y (line N-S); the principle compression stress components (P-axis) expand from the area of plus or minus 30 degrees by the direction of Z-axis (point W or point E) to the direction of plane X-Y (line N-S) further and finally form an obvious phenomenon of regular arrangement in some local area; inside each multijoint sample, there are obvious crescent regular arrangements near 30 to 60 degrees by the direction

of Z-axis (point W or point E), which illustrates that the multijoint structure can affect the fracture orientation of acoustic emission events to a certain extent; the principle stress components (T-axis) expand from the direction of plane X-Y (line N-S) to Z-axis (point W or point E).

In conclusion, we can obtain the large number of mesoscopic fracture characteristics of acoustic emission events such as dimensional orientation, failure status, failure type, and moment magnitude in the progress of rock failure to study the failure mechanism of joint rock and macro-evolution law of joint rock by utilizing the method of moment tensor inversion P-T diagram and T-k diagram. It can provide a new means to analyze the stability and the development tendency of rock and is an effective supplement to traditional methods.

## Data Availability

The data used to support the findings of this study are included within the article.

## Conflicts of Interest

The author declares that there are no conflicts of interest regarding the publication of this paper.

## Acknowledgments

This work was supported by the Major Systematic Project of Science and Technology Research and Development Plan of China National Railway Group Co., Ltd. (no. P2019G001) and the Scientific Research Foundation of China Academy of Railway Sciences Group Co., Ltd. (no. 2018YJ030).

## References

- [1] D. Lockner, "The role of acoustic emission in the study of rock fracture," *International Journal of Rock Mechanics and Mining Sciences & Geomechanics Abstracts*, vol. 30, no. 7, pp. 883–899, 1993.
- [2] J. Kaiser, *An Investigation into the Occurrence of Noises in Tensile Tests or a Study of Acoustic Phenomena in Tensile Tests*, Technische Hochschule–München, Munich, Germany, 1950.
- [3] F. B. Liu and Y. M. Cheng, "The improved element-free Galerkin method based on the nonsingular weight functions for inhomogeneous swelling of polymer gels," *International Journal of Applied Mechanics*, vol. 10, no. 4, pp. 1–25, 2018.
- [4] F. B. Liu, Q. Wu, and Y. M. Cheng, "A meshless method based on the nonsingular weight functions for elastoplastic large deformation problems," *International Journal of Applied Mechanics*, vol. 11, no. 1, Article ID 1950006, 2019.
- [5] H. Cheng, M. J. Peng, and Y. M. Cheng, "A fast complex variable element-free Galerkin method for three-dimensional wave propagation problems," *International Journal of Applied Mechanics*, vol. 9, no. 6, Article ID 1750090, 2017.
- [6] F. X. Sun, C. Liu, and Y. M. Cheng, "An improved interpolating element-free galerkin method based on nonsingular weight functions," *Mathematical Problems in Engineering*, vol. 2014, Article ID 323945, 13 pages, 2014.
- [7] T. Ishida, "Acoustic emission monitoring of hydraulic fracturing in laboratory and field," *Construction and Building Materials*, vol. 15, no. 5-6, pp. 283–295, 2001.
- [8] E. N. Landis, "Micro-macro fracture relationships and acoustic emissions in concrete," *Construction and Building Materials*, vol. 13, no. 1-2, pp. 65–72, 1999.
- [9] M. Ohtsu, "Acoustic emission theory for moment tensor analysis," *Research in Nondestructive Evaluation*, vol. 6, no. 1, pp. 169–184, 1995.
- [10] K. Ohno and M. Ohtsu, "Crack classification in concrete based on acoustic emission," *Construction and Building Materials*, vol. 24, no. 12, pp. 2339–2346, 2010.
- [11] S. Muralidhara, B. K. R. Prasad, H. Eskandari, and B. L. Karihaloo, "Fracture process zone size and true fracture energy of concrete using acoustic emission," *Construction and Building Materials*, vol. 24, no. 4, pp. 479–486, 2010.
- [12] M. C. He, J. L. Miao, and J. L. Feng, "Rock burst process of limestone and its acoustic emission characteristics under true-triaxial unloading conditions," *International Journal of Rock Mechanics and Mining Sciences*, vol. 47, no. 2, pp. 286–298, 2010.
- [13] C. Li and E. Nordlund, "Experimental verification of the Kaiser effect in rocks," *Rock Mechanics and Rock Engineering*, vol. 26, no. 4, pp. 333–351, 1993.
- [14] F. Gilbert, "Excitation of the normal modes of the earth by earthquake sources," *Geophysical Journal International*, vol. 22, no. 2, pp. 223–226, 1971.
- [15] H. G. Ji, H. W. Wang, S. Z. Cao, and Z. Hou, "Experimental research on frequency characteristics of acoustic emission signals under uniaxial compression of granite," *Chinese Journal of Rock Mechanics and Engineering*, vol. 31, pp. 2900–2905, 2012.
- [16] X. D. Zhao, C. A. Tang, Y. H. Li, and R. Yuan, "Study of AE activity characteristics under uniaxial compression loading," *Chinese Journal of Rock Mechanics and Engineering*, vol. 25, no. 22, pp. 3673–3678, 2006.
- [17] X. D. Zhao, Y. H. Li, R. F. Yuan, and T. Yang, "Study on crack dynamic propagation process of rock samples based on acoustic emission location," *Chinese Journal of Rock Mechanics and Engineering*, vol. 26, no. 5, pp. 944–950, 2007.
- [18] X. D. Zhao, J. P. Liu, Y. H. Li, J. Tian, and W.-C. Zhu, "Experimental verification of rock locating technique with acoustic emission," *Chinese Journal of Geotechnical Engineering*, vol. 30, no. 10, pp. 1472–1476, 2008.
- [19] P. S. Chen, "Seismic moment tensor and its inversion," *Seismological and Geomagnetic Observation and Research*, vol. 16, no. 5, p. 19, 1995.
- [20] B. Feignier and R. P. Young, "Moment tensor inversion of induced microseismic events: evidence of non-shear failures in the  $-4 < M < -2$  moment magnitude range," *Geophysical Research Letters*, vol. 19, no. 14, pp. 1503–1506, 1992.
- [21] J. F. Hazzard and R. P. Young, "Moment tensors and micromechanical models," *Tectonophysics*, vol. 356, no. 1–3, pp. 181–197, 2002.
- [22] J. F. Hazzard and R. P. Young, "Dynamic modelling of induced seismicity," *International Journal of Rock Mechanics and Mining Sciences*, vol. 41, no. 8, pp. 1365–1376, 2004.
- [23] A. Y. Cao, *Research on Seismic Effort of Burst and Failure of Coal-Rock Mass Associated with Mining and its Application*, China University of Mining and Technology, Xuzhou, China, 2009.
- [24] J. F. Chai, A. B. Jin, Y. T. Gao, and S. C. Wu, "Water inrush inoculation process in mines based on moment tensor inversion," *Chinese Journal of Engineering*, vol. 37, no. 3, p. 267, 2015.

- [25] J. F. Chai, A. B. Jin, and S. C. Wu, "Rock fracture mechanism and its evolution law of triaxial compression test based on P-T distribution diagram method," *Electronic Journal of Geotechnical Engineering*, vol. 20, no. 28, pp. 13451–13464, 2015.
- [26] J. F. Chai, A. B. Jin, and S. C. Wu, "Mechanism and evolution law of rock failure based on moment tensor inversion," *Electronic Journal of Geotechnical Engineering*, vol. 20, no. 15, pp. 6659–6672, 2015.
- [27] J. F. Chai, Y. T. Gao, S. C. Wu, and Y. Zhou, "Research on single jointed rock failure mechanism based on mesoscopic characteristics analysis," *Journal of Mining and Safety Engineering*, vol. 33, no. 3, pp. 528–534, 2016.
- [28] F. Liu and Y. Cheng, "The improved element-free Galerkin method based on the nonsingular weight functions for inhomogeneous swelling of polymer gels," *International Journal of Applied Mechanics*, vol. 10, no. 4, Article ID 1850047, 2018.
- [29] F. Liu, Q. Wu, and Y. Cheng, "A meshless method based on the nonsingular weight functions for elastoplastic large deformation problems," *International Journal of Applied Mechanics*, vol. 11, no. 1, Article ID 1950006, 2019.
- [30] Q. Wu, F. B. Liu, and Y. M. Cheng, "The interpolating element-free Galerkin method for three-dimensional elastoplasticity problems," *Engineering Analysis with Boundary Elements*, vol. 115, pp. 156–167, 2020.
- [31] S. Y. Yu, M. J. Peng, H. Cheng, and Y. M. Cheng, "The improved element-free Galerkin method for three-dimensional elastoplasticity problems," *Engineering Analysis with Boundary Elements*, vol. 104, pp. 215–224, 2019.
- [32] K. Aki and P. G. Richards, *Quantitative Seismology: Theory and Methods*, Vol. 1, W. H. Freeman, San Francisco, CA, USA, 2nd edition, 1980.
- [33] J. A. Hudson, R. G. Pearce, and R. M. Rogers, "Source type plot for inversion of the moment tensor," *Journal of Geophysical Research*, vol. 94, no. B1, pp. 765–774, 1989.